Intercomparison of dual-polarization X-band mini-radar performances with reference radar systems at X and C band in Rome supersite

Stefano Barbieri

Stefano Barbieri[1], Errico Picciotti[1,3], Mario Montopoli[1,2], Saverio Di Fabio[1], Raffaele Lidori[1]
Frank Marzano[1,2], John Kalogiros[4], Marios Anagnostou[4] and Luca Baldini[5],

[1]*CETEMPS, University of L'Aquila, Via Vetoio, L'Aquila, 67100, Italy*
[2]*Department of Electronic Engineering, DIET, Sapienza University of Rome, Italy*
[3]*Himet s.r.l. srl, SS 17 Ovest n.36, L'Aquila, Italy*
[4]*NOA National Observatory of Athens, Athens ,Greece*
[5]*Institute of Atmospheric Sciences and Climate, CNR ISAC, Roma, Italy*
(Dated: 15 July 2014)

1 Introduction

In recent years, new developments on X-band dual-polarization technology have received the interest of scientific and operational communities (*Bringi and Chandrasekar, 2001*). New efforts are now focusing on the optimization of cost, benefit and performance of low-power and compact X-band system as well as their use in a network configuration (*McLaughlin et al., 2009*). It is well known that their limitations, with respect to S/C band fixed traditional weather radar systems, are the smaller coverage due to low transmission power and the significant signal attenuation experienced at X-band in heavy rain (*e.g., Tabary et al., 2008*).

Within the context above, an innovative dual-polarization X-band mini radar system managed by Himet srl (hereafter called MiniPolX) was tested during and after the Special Observation Period (SOP1), part of the HyMeX experimental campaign (Hydrological cycle in the Mediterranean Experiments) (*Ferretti et al., 2014*). During the extended SOP1 period within fall and winter of 2012-2013, MiniPolX dual-polarized observations of Z_h, ρ_{hv}, K_{dp} and Z_{dr} were evaluated against other two polarimetric radars used as benchmark systems. These two reference radars are the National Observatory of Athens' X-band (XPOL) mobile system and the National Research Council (CNR)'s C-band (Polar 55C) dual polarization system.

This evaluation is obtained after applying the same Radar Advanced Polarimetric Processing (RAPP) chain to the three systems used in the analysis. The RAPP chain has been developed for this study, and its preliminary performance was evaluated by means a comparative analysis between MiniPolX rain estimation and in-situ rain measurements from gauges network.

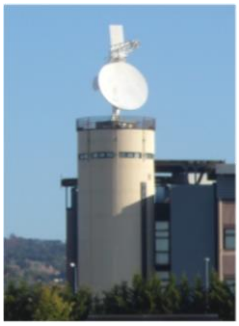

Features	Units	MiniPolX	Polar 55C	XPOL
Frequency	[GHz]	9.41	5.6-5.65	9.37
Peak Power	[kW]	25	500	60
Antenna Gain	[dB]	35	45.5	40
Maximum Range	[km]	120	200	120
Gate resolution	[m]	250	75	150
Beamwidth	[deg]	3	0.92	0.9
Elevations angles used in PPI scans	[deg]	1, 2, 3, 4, 5, 10	0.6, 1.6, 2.5, 4.0, 5.5, 7.5, 9.5, 12.0	1, 2, 3

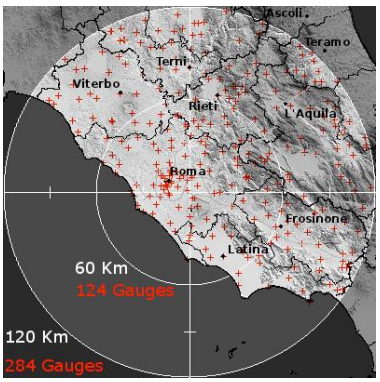

Figure 1: Pictures of MiniPolX (left), Polar 55C (center), and XPOL (right) taken at ISAC-CNR premises in Rome (top). Their specifications (bottom, left) and coverage area during measurement campaign (bottom, right). Gauges distribution is shown for completeness with red circle on the bottom right panel.

2 Experimental campaign setup

The measurement field campaign in the Rome area, took place from September 2012 to March 2013 extending the period of SOP1-HyMeX which ended on Nov. 6, 2012. During this period a large data set composed by 53 rainy events occurred in the Central Italy has been collected. XPOL and MiniPolX were installed within 300-meter distance in the Tor Vergata research area where ISAC-CNR is hosted and where Polar 55C is permanently located.

The ISAC-CNR experimental site is located 15 km South-East of Rome (lat. 41°50'24" N, lon. 12°38'50" E, 102 m ASL). During the study period, a continuous acquisition was carried out using PPI scans at different elevation angle with 10 minutes temporal resolution. Hourly rain accumulations were acquired by a dense network of 124 rain gauges and used in the analysis as ground reference (Figure 1).

3 Radar data processing

The radar observations used in this analysis are the horizontal reflectivity Z_h, the differential reflectivity Z_{dr}, the differential phase shift Φ_{dpm} and correlation coefficient ρ_{hv}. The comparison among radar variables with different spatial sampling features, as in our case, has to be carefully tackled, since the lack of a preliminarily spatial adaptation may lead to incorrect conclusions.

To this goal, raw data at finer resolution from Polar 55C and XPOL have been adapted to the coarser resolution of MiniPolX. The approach adopted foresees the selection of the high resolution sampling volumes (V_{HR}) of the Polar 55C or XPOL, which lie within the nearest low resolution sampling volume (V_{LR}) of MiniPolX. Then, the average of the considered radar quantity at V_{HR} scale is performed to obtain the same quantity at V_{LR} scale (Figure 2). This is practically implemented taking averages along azimuth, range and elevation directions. Additionally, in order to minimize possible smoothing effects on the vertical profile of reflectivity (VPR), which compensation is not taken into account, the analysis is restricted to ranges less than 60 km from the radar.

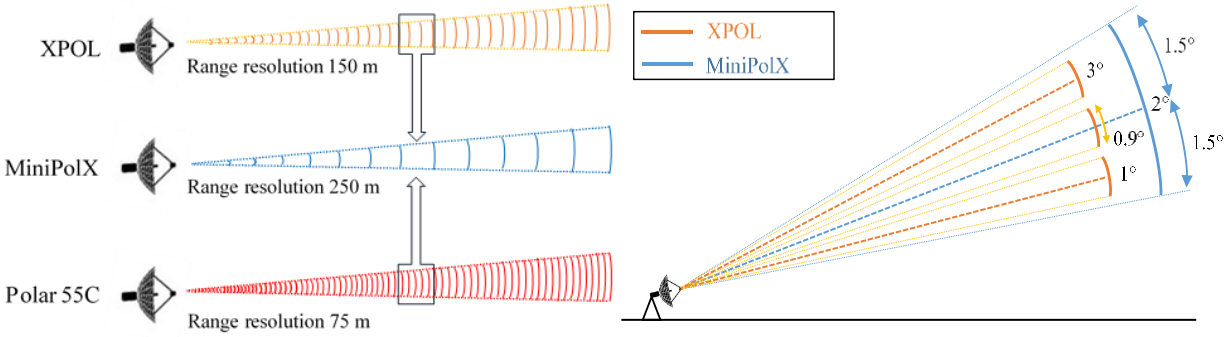

Figure 2: Sketch of XPOL and Polar 55C adaptation to MiniPolX range resolution (left) and to beamwidth resolution (right)

After accomplishing the spatial adaptation of the radar variables of the three systems, the RAPP processing chain is applied to each data volume. Figure 3 shows the block diagram of the RAPP steps implemented as detailed in the following sections.

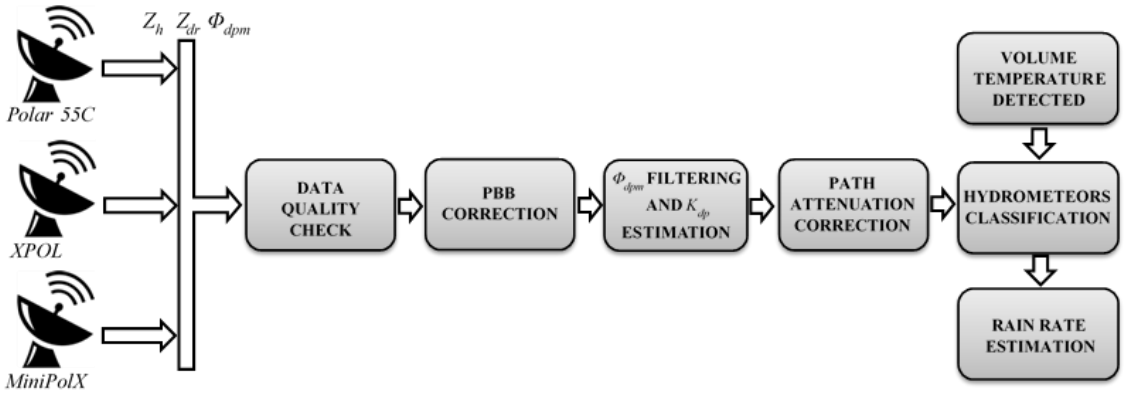

Figure 3: Radar advanced polarimetric processing (RAPP) processing chain's block diagram

3.1 Data quality check

The first step of the RAPP algorithm chain is the quality check methodology applied to flag radar observables as good or bad. Data quality has been estimated through polarimetric self-consistency (*Straka et al. 2000*), while ground-clutter and WLAN interference has been removed by exploiting the textural spatial correlation of meteorological targets with respect to artifacts: differential reflectivity is subject to fluctuations, abrupt variations, typically of the order of few dBs, which would

provide noisy trends with excessive oscillations between positive and negative. A median smoothing filter (MSF) was applied to Z_{dr}, sliding through the signal, pixel by pixel, with a window of 2 km, and replacing each bin with the median of neighboring bins content in the window.

3.2 Partial beam blockage correction

The second step of the processing chain is the partial beam blockage (PBB) correction. When a radar beam intercepts a mountain, two situations are possible: 1) only part of the beam cross section illuminates the intercepted topography (partial blockage), or 2) the radar beam is completely blocked (total blockage). An occlusion of the beam of the order of less than 10% is considered negligible and is not corrected while an occlusion that exceeds 60% is rejected. If radar bins are partially shielded between 10% and 60% the radar equivalent reflectivity factor measurements is modified by adding 1-4 dB depending on the degree of occultation (*Fulton et al. 1998*).

3.3 Differential phase filtering and K_{dp} estimation

The operation of phase filtering (smoothing) consists of applying to the differential phase a filter function whose purpose is to highlight the precipitation samples, attenuating the noise generated from environmental artifacts, or other disturbing phenomena (*Bringi and Chandrasekar, 2001*).

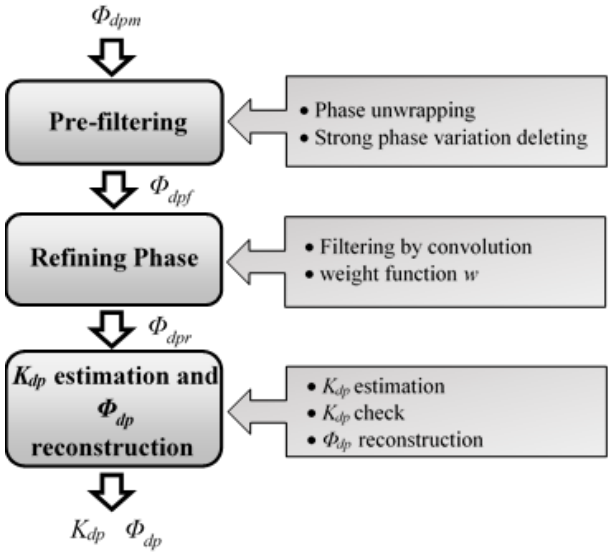

Figure 4: Block diagram describing the applied procedure for Φ_{dpm} filtering and K_{dp} retrieval

A multistep moving-window range derivative approach is applied to the differential phase measured (Φ_{dpm}) which includes the backscattering differential phase and can be summarized in three main steps (similar to *Vulpiani et al. 2012*) as shown in Figure 4:

In the pre-filtering step, two algorithms are applied: the unwrapping algorithm allows to obtain a continuous phase signal, free from 2π jumps, from a wrapped phase signal; while the mitigation of strong phase variation removes the samples whose phase difference with adjacent samples is higher than a threshold of 20°.

The second step is to filter the pre-filtered signal Φ_{dpf} using a convolution approach. A triangular transfer function is used to run the convolutional filter. Its window size (M) varies between 4 and 6 km.

With respect to the K_{dp} retrieval, the latter is reconstructed from Φ_{dpr} after the step of convolution filtering, through a finite-difference scheme over a given-sized moving window that is:

$$K_{dp}(r_k) \approx 0.5 \frac{\left[\Phi_{dpr}\left(r_k + \frac{L}{2}\right) - \Phi_{dpr}\left(r_k - \frac{L}{2}\right)\right]}{L} \qquad (3.1)$$

where L = 6 km. The reconstructed differential phase shift at range gate r_k is as follows:

$$\Phi_{dp}(r_k) = 2\sum_{r_0}^{r_k} K_{dp}(r_i)\,\Delta r \qquad (3.2)$$

Note that, in general, the length of the windows M and L for phase filtering and K_{dp} estimation may differ, but in this case they are both fixed at the same value (6 km) for each radar system.

Figure 5 shows a sample of range profile of filtered K_{dp} and Φ_{dpm} from Polar 55C, XPOL and MiniPolX at 1° elevation. Profiles refer to an event occurring January 23, 2013 at around 9:40 UTC. A peak in the K_{dp} profile, located around 40 km from the radars (Figure 5: right panel), identifies a weather event rather intense. The K_{dp} peaks show a mismatch in range at approximately 40 km. The reason for this behavior may be due to precipitation cell which moves toward the radar. From the scan time series and from the extent of the mismatch, we have estimated a radial velocity around 45 km/h or about 12.5 m/s, very similar to that provided by XPOL data for which the estimated radial velocity is of 14 m/s or about 50 km/h.

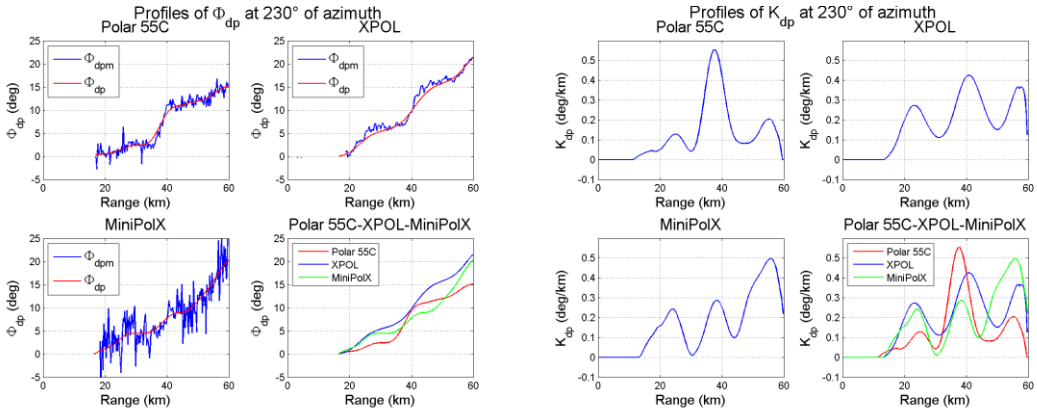

Figure 5: Polar 55C, XPOL and MiniPolX Φ_{dp} (left panel) and K_{dp} estimation (right panel)

3.4 Path attenuation correction

At X-band frequencies path attenuation of radar signal by rain can be quite significant with values greater than 10 dB in heavy rain (*Kalogiros et al., 2014*). Attenuation correction algorithm (*Bringi and Chandrasekar, 2001*) is applied to Z_h and Z_{dr} by using Φ_{dp} which is filtered as described in previous section:

$$Z_{hc} = Z_h + dZ_h = Z_h + \alpha\left[\Phi_{dp}(r_N) - \Phi_{dp}(r_0)\right] \qquad Z_{drc} = Z_{dr} + dZ_{dr} = Z_{dr} + \beta\left[\Phi_{dp}(r_N) - \Phi_{dp}(r_0)\right] \qquad (3.3)$$

where α = 0.28, β = 0.04 for X-band (*Tabary et al. 2008*) and α = 0.08, β = 0.03 for C-band (*Gourley et al. 2007*). The rain attenuation correction algorithm was applied to all radars for all the collected data set. Figure 6 (top) shows an example of horizontal reflectivity (Z_h) PPI map at approximately the same time during the rain event of January 23, 2013. XPOL has no data in the azimuth sector from 107° to 195° for the presence of the cab of the vehicle on which the radar is mounted (Figure 1). For consistency, both in the MiniPolX and in the Polar 55C, the same sector has not been considered. The attenuation correction factor, as showed in Figure 6 (bottom panel), reaches up to 8 dB at X-band, while it is quite moderate at C-band where it reaches up to 2.2 dB. As expected the attenuation at C band is lower than that obtained at X band and, after its compensation, the values of reflectivity seems to be more consistent to each other and ready to be used in the rain retrieval scheme, as discussed later on.

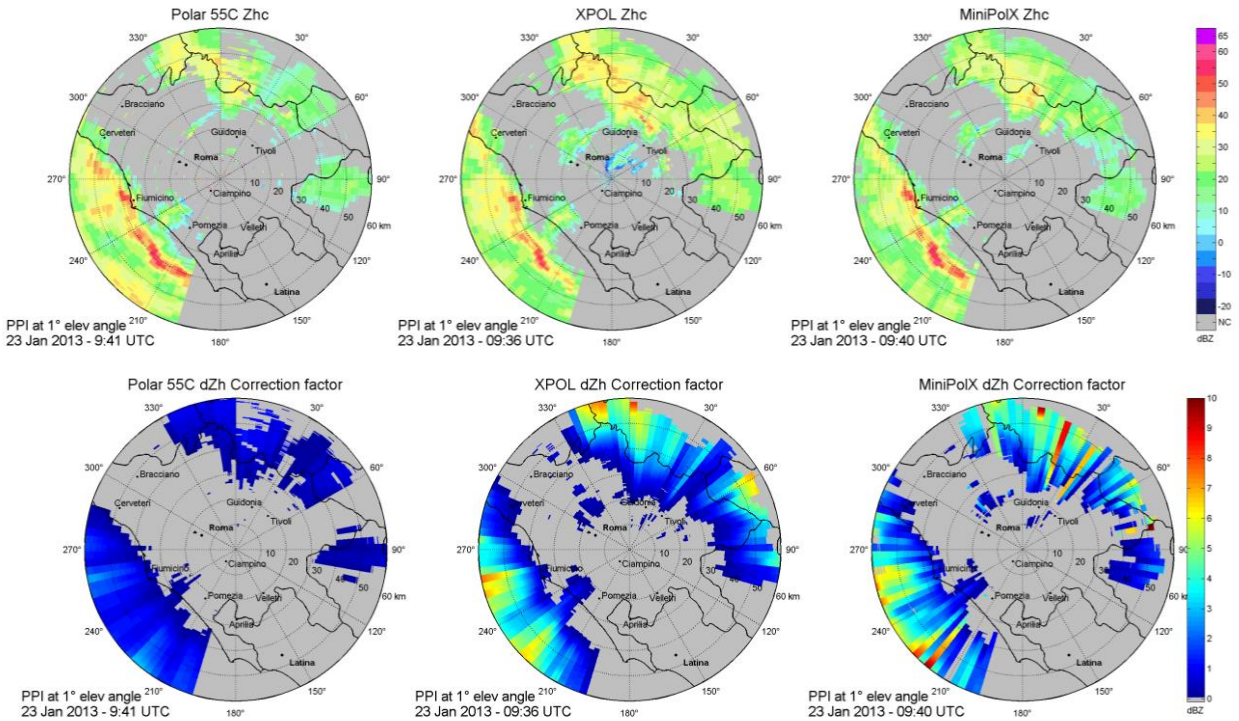

Figure 6: Polar 55C, XPOL and MiniPolX Z_h corrected for attenuation (upper panel) and the relative correction factor (bottom)

3.5 Hydrometeors classification

The hydrometeor classification is based on a Bayesian algorithm (*Marzano et al, 2010*), trained with a radar backscattering-model simulations based on the T matrix code (*Mishchenko et al., 1998*) where liquid, ice and mixed phase hydrometeors are simulated. Simulations can take into account composition, shape, size, canting angle and dielectric properties of hydrometeors in different phases and using as input Z_h, Z_{dr}, K_{dp} and the temperature T.

The hydrometeor classification maps from both C- and X-band at two elevation angles are shown in Figure 7 for the case of January 23, 2013, 09:40 UTC where the 10 hydrometeor classes are color coded. The maps at 1° elevation (top panel) show that all sectors, up to a distance of about 50 km, are characterized mainly by light rain with some differences between C- and X-bands in the N and SW sectors. The transition from the hydrometeor liquid to solid state identifies the freezing level, located, for the analyzed case at an altitude of about 1200 m, while the small hail cap has a well distinct signature with some embedded wet snow. The maps at 2° elevation (bottom panel) show that all sectors, up to a distance of about 30 km, are characterized mainly by light rain with some differences between C- and X-bands in the SW sector. The transition from the liquid to solid state identifies the freezing level, located at an altitude of about 1200 m. The ice crystal cap has a well distinct signature with some embedded dry snow. The wet snow transition between the rain portion and the ice-crystal region is clearly detected, even if it is in different sectors in the C- and X-bands classification maps.

Note that, the qualitative analysis of the classified maps shows a substantial agreement in the dual-polarization observables of the 3 radar systems when they are used for hydrometeor classification.

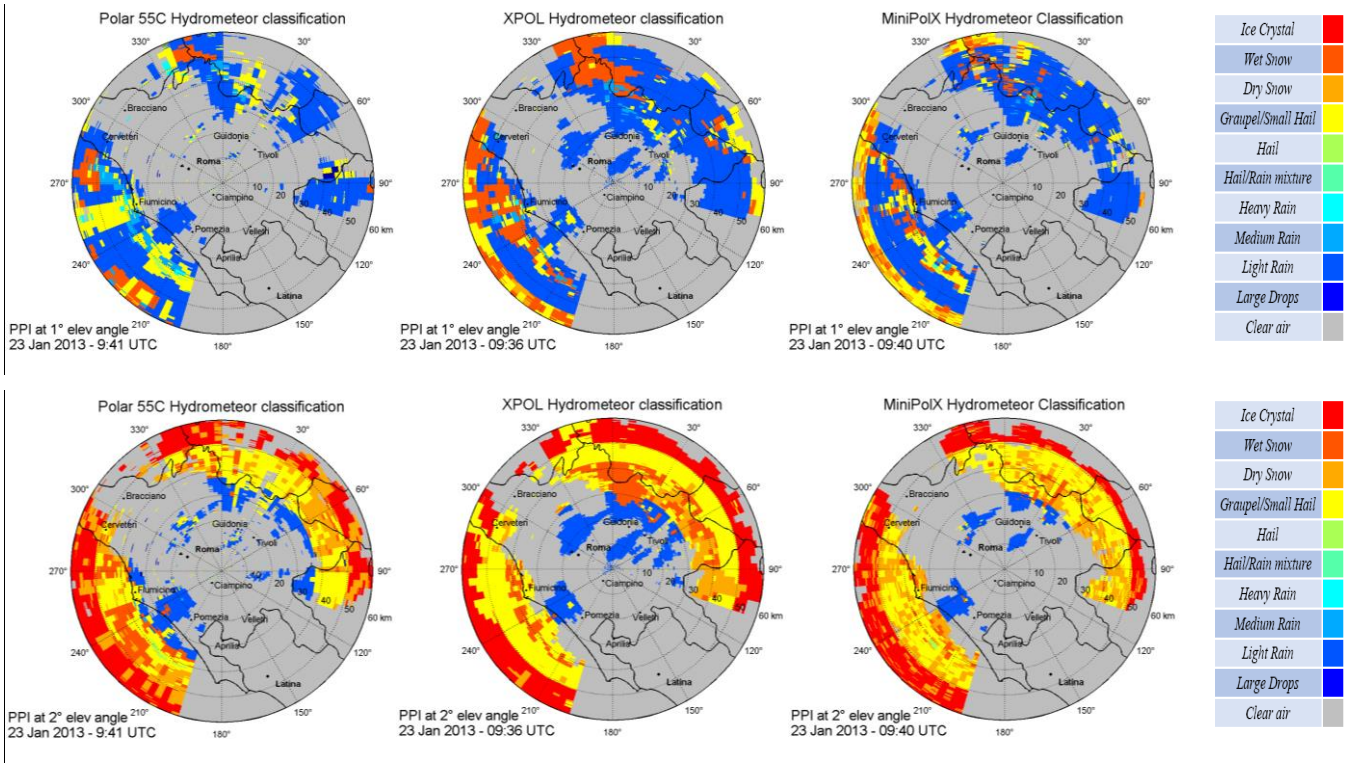

Figure 7: Polar 55C (left), XPOL (central) and MiniPolX (right) PPI of hydrometeor classification at 1° elevation (top panel) and 2° elevation (bottom panel), measured on January 23, 2013, at around 09:40 UTC.

3.6 Rainfall estimation

For each radar system near-surface rainfall rate is computed from the lowest bin measurement (LBM) or vertical maximum intensity (VMI) products by mean four types of estimators, derived by Bringi and Chandrasekar (2001):

1) $R(Z_h) = \left(10^{\frac{Z_h}{10}}\right)^{1/b} \left(\frac{1}{a}\right)^{1/b}$ with $\boldsymbol{a}$ = **443.5** and $\boldsymbol{b}$ = **1.2987** for X band and $\boldsymbol{a}$ = **200** and $\boldsymbol{b}$ = **1.60** for C-band

2) $R(K_{dp}) = a \cdot \left(|K_{dp}|\right)^b \cdot \mathrm{sign}(K_{dp})$ with $\boldsymbol{a}$ = **19.18** and $\boldsymbol{b}$ = **0.85** for X band and $\boldsymbol{a}$ = **20.5** and $\boldsymbol{b}$ = **0.96** for C-band

3) $R(Z_h, Z_{dr}) = a\left(10^{\frac{Z_h}{10}}\right)^b \left(10^{\frac{Z_{dr}}{10}}\right)^c$ with $\boldsymbol{a}$ = **0.0039** $\boldsymbol{b}$ = **1.07** $\boldsymbol{c}$ = **-5.97** for X-band and $\boldsymbol{a}$ = **0.0058** $\boldsymbol{b}$ = **0.91** $\boldsymbol{c}$ = **-2.09** for C-band

4) $R(K_{dp}, Z_{dr}) = a \cdot \mathrm{sign}(K_{dp}) \cdot |K_{dp}|^b \left(10^{\frac{cZ_{dr}}{10}}\right)$ with $\boldsymbol{a}$ = **28.6** $\boldsymbol{b}$ = **0.95** $\boldsymbol{c}$ = **-1.37** for X-band and $\boldsymbol{a}$ = **30.1** $\boldsymbol{b}$ = **0.933** $\boldsymbol{c}$ = **-0.74** for C-band

where Z_h, Z_{dr}, K_{dp} and R in dBZ, dB, °/km and mm/h, respectively.

For X-band radars, a new optimal algorithm to estimate the parameters of the rain drop size distribution (DSD), the mean drop shape, and rainfall rate (*Kalogiros et. al 2013*) has been also adopted.
An example of rain rate output is shown in Figure 8 where 2 types of estimators for MiniPolX are compared with XPOL estimation. When compared to XPOL rain estimates, it seems that $R(Z_h, Z_{dr})$ MiniPolX estimates perform adequately well.

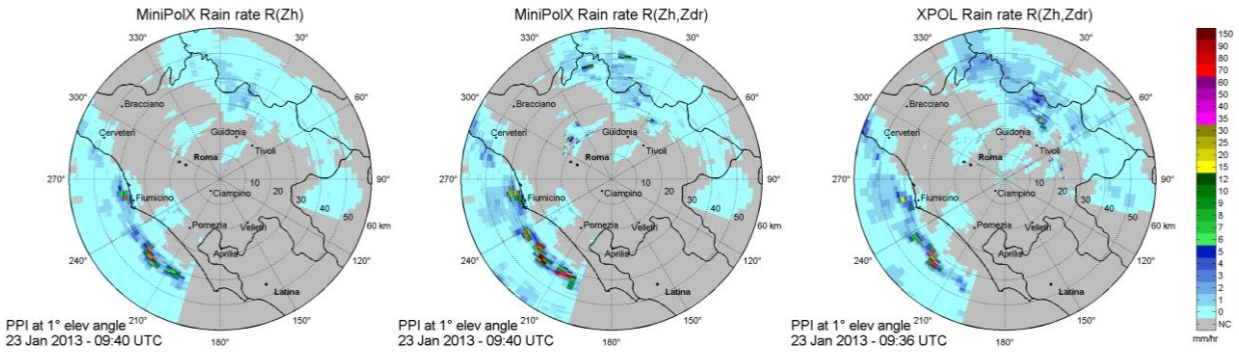

Figure 8: MiniPolX rain rate estimation using $R(Z_h)$ (left) and $R(Z_h, Z_{dr})$ (center). Also the XPOL estimation using $R(Z_h, Z_{dr})$ is shown for qualitive comparison.

4 Comparison of polarimetric variables

The MiniPolX radar observables, Z_h, Z_{dr} and ρ_{hv}, have been compared with the corresponding XPOL and Polar 55C polarimetric variables, used as benchmark systems. The accuracy of the MiniPolX polarimetric observations have been quantified by introducing the error ε_P defined as difference between XPOL and MiniPolX polarimetric measurements: $\varepsilon_P = \left(P_{XPOL} - P_{MiniPolX}\right)$ where P indicates a radar variable. Then the error $Bias = \langle \varepsilon_P \rangle = \langle P_{XPOL} - P_{MiniPolX} \rangle$ where angle brackets is the ensemble averaging in time and space. Moreover, correlation coefficient (*Corr*), standard deviation (*Std*) and the root mean square error normalized in percentage to the range of the observed data (*NRMSE*) have been calculated. In a similar manner Polar 55C and MiniPolX data were compared.

Figure 9 shows the results at 1° elevation for Z_h and Z_{dr} for the whole day of January 23, 2013. Similar results have been obtained for other elevations and events. Despite the changes due to the spatial adaptation process from XPOL and Polar 55C to MiniPolX resolution, the comparison shows a good correspondence between the three radars. Note that we did not applied any frequency scaling for the comparison of X and C band reflectivity data. In this respect it is notable the quite good agreement between Polar 55C and MiniPolX, also owing to the spatial adaptation we performed among the system.

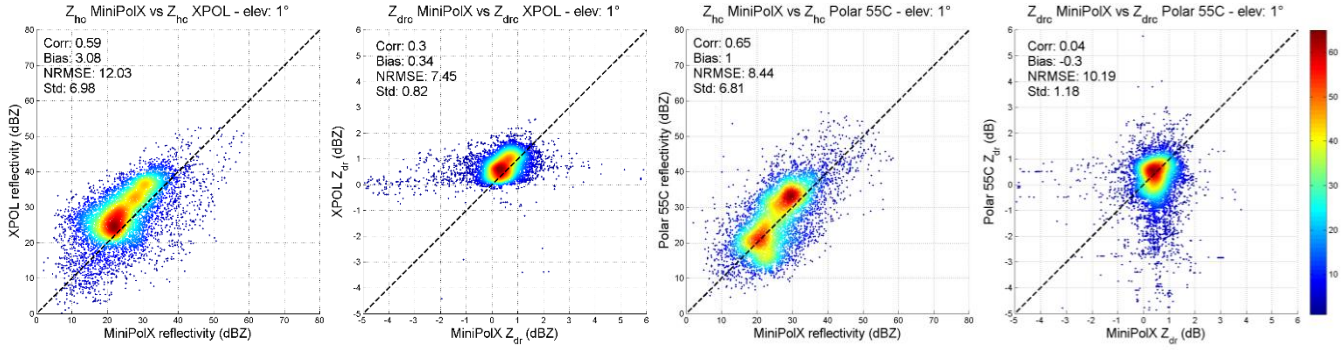

Figure 9: Scatter plots of corrected Z_h, and Z_{dr} utilizing 1° elevation data for January 23, 2013 case study.

The scatter plot of ρ_{hv} between XPOL and MiniPolX is shown in Figure 10 (left panel). It is quite evident the lower value of MiniPolX with respect XPOL mainly due to the MiniPolX decrease in performance at long range, as shown in Figure 10 (blue line in right panel). The main reasons of the difference are probably due to the noise figure, to a residual clutter in the 3-deg beam or to a higher non-uniform beam-filling (NUBF) related to a lower beam resolution.

The latter, caused by a wider beamwidth, is more pronounced far away from the radar when the sampling volumes become large enough to include different species of reflecting particles or when the sampling volumes are not completely filled by the reflecting particles. Note that a special case of NUBF occurs when sampling volumes are within the bright band so that minima of ρ_{hv} are registered. For the case in Figure 10, the abrupt decrease of ρ_{hv} at 40 km is probably not due to bright band because from the hydrometeor classification in Figure 7, the melting layer is expected to be at approximately 55 km from the radar when ray paths at 1° elevation are analyzed.

It is worth noting that ρ_{hv} is partly compensated by applying the following relation (*Bringi and Chandrasekar, 2001*):

$$\rho_{hv\_comp} = \rho_{hv}(1 + 10^{-0.1SNRdB}) \quad \text{with} \quad SNRdB = C_{SNRdB} + Z_{hc} - 20log_{10}(r) \qquad (4.1)$$

where C_{SNRdB} is a constant (in dB) defined as $10log_{10}(C_{rad}P_n^{-1})$, C_{rad} is the radar constant and P_n the noise power, while r is the distance from the radar position (in km) of a given radar bin. The improvement of the behavior of ρ_{hv} compensated is quantified by the indices of error in which there is a reduction of the Bias of about 36%, and a reduction of the NRMSE of 14.6%.

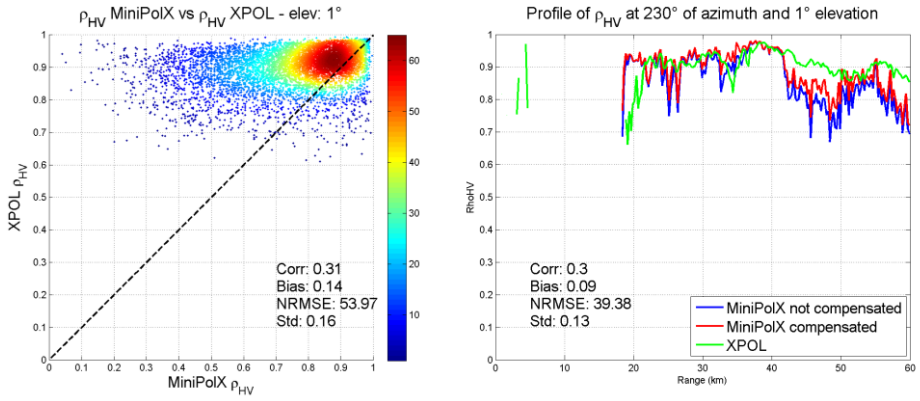

Figure 10: Scatter plots of ρ_{hv} before the compensation (left panel) and range profiles of ρ_{hv} before and after the compensation, also the error indexes after compensation are shown for completeness (right panel)

5 Processing chain performance

The rainfall events, occurred during the 2012-13 experimental campaign, were used to illustrate the performance of the processing chain applied to MiniPolX unit over the city of Rome. The ground observations from the network of 124 rain gauges (see in Figure 1 for their location) is provided by the Italian Department of Civil Protection. A quality-controlled methodology has been applied to the available dataset in order to consider only gauges with reliable data so that, after implementing the correction procedure, rain-gauge measurement errors are assumed to be negligible with respect to the radar bias.

For the quantitative analysis of radar estimates and rain gauges only the relation $R=R(Z_h)$ given in section 3.6, has been used. In particular, Z_h is extracted from VMI of each available radar volume and then is converted from polar to Cartesian regular grid with spacing of 0.250 km. For each rain gauge we have selected the radar rain rate estimate closest to the value recorded by the rain gauge within an area of 0.5x0.5 km^2 around the gauge position. About 20 heterogeneous rainy events including severe thunderstorms, convective lines, wide spread stratiform rainfalls and cold front systems have been analyzed.

The hourly radar-derived rain estimation (R) and hourly gauge observations (G), expressed in mm, were compared after introducing the retrieval error which is defined as $\varepsilon_G = R - G$. By indicating again with the angle brackets the ensemble averaging in time and space, the following score indexes have been used: i) Multiplicative Bias $MB = \langle R/G \rangle$ whose optimal value is 1; ii) the Root mean square Error $RMSE = \sqrt{\langle \varepsilon_G^2 \rangle}$ whose optimal value is 0 and the Correlation Coefficient CC whose optimal value is 1. Three version of the $R(Z_h)$ rain estimator derived from MiniPolX data, are compared:

- $R_1=R(Z_h)$ by using measured reflectivity (after applying data quality check step only)
- $R_2=R(Z_{hc})$ by using reflectivity corrected by the processing chain
- $R_3=R(Z_h)\cdot F(r)$ by using measured reflectivity whose estimation is corrected by a range adjustment factor F

R_3 is used as a benchmark; in fact, the propagation of the radar beam for the antenna elevations greater than zero in a standard atmosphere suggests that an underestimation of surface rain field is likely at longer ranges due to both the increasing height of the sampled atmospheric volume and to the two-way path attenuation. This issue can be partially overcome by introducing an explicit range adjustment function $F(r)$ computed by means of radar-gauge comparison (*Picciotti et al. 2008*).

Figure 11 shows MB as a function of the distance from the radar for R_1, R_2, R_3. From the blue curve of Figure 11, it appears evident the underestimation of $R_1=R(Z_h)$ for increasing distances. This *range-dependent* effect can be compensated introducing an adjustment factor $F(r)$ which can be modeled as a polynomial or exponential fit for the MiniPolX:

$$F(r) = a\,r^3 + b\,r^2 + c\,r + d \quad with \;\; a = -2.15 \cdot 10^{-6} \;\; b = 9.57 \cdot 10^{-4} \;\; c = -4.39 \cdot 10^{-2} \;\; and \;\; d = 1.76 \qquad (5.1)$$

In the same figure exists an appreciable difference of MB and RMSE between R_1 and R_2 estimators. The performance of R_2 is also better than R_3 up to 45 km from radar site, beyond that the effect of distance becomes predominant. Better scores of R_2 are also confirmed by the overall error analysis (taking into account all rainy events) for hourly cumulated rainfall as

shown in table 1. It is interesting to note the similar overall behavior of R_2 and R_3, meaning that our RAPP algorithm chain (in particular the attenuation compensation), when applied to MiniPolX variables, produces similar results to those obtained without using any special processing, but adapting radar-derived rain estimates to those of the gauge ground reference on event basis. Of course, the latter choice requires the simultaneous processing of two sources of information (radar and gauge network), while the former is self-consistent (polarimetric radar only).

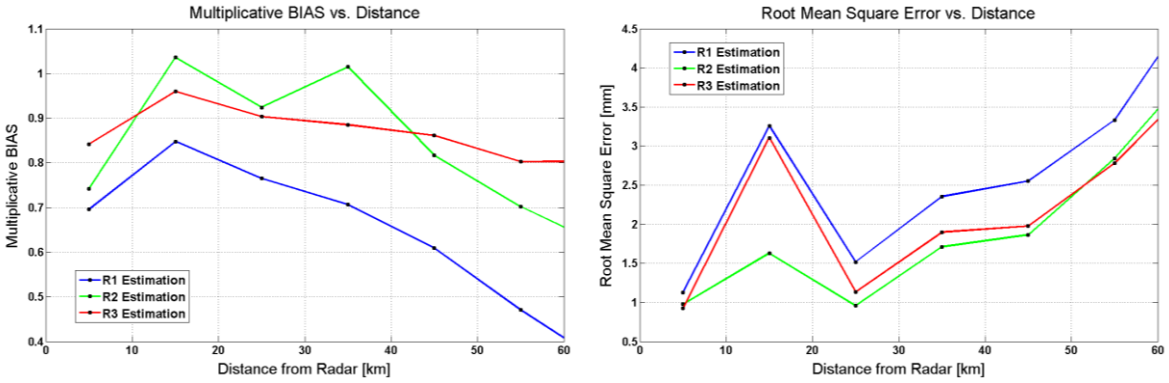

Figure 11: Multiplicative Bias (left) and RMSE (right) as a function of distance for the three rain estimation

Table 1: Overall error scores computed for hourly cumulated rainfall.

	Rain Estimation from MiniPolX		
Error Indexes	***R1***	***R2***	***R3***
Root Mean Square Error (RMSE)	2.6764	1.9272	2.2672
Multiplicative BIAS (MB)	0.6678	0.8867	0.8454
Correlation Coefficient (CC)	0.7582	0.8591	0.8046

The effect of the RAPP chain correction appears quite significant by looking at Figure 12 where 24-hour MiniPolX accumulated derived from R_1 and R_2 estimation are compared with rain-gauge interpolation for a case study. The quality of interpolated gauge maps (holes, rain pattern etc.) depends on both the interpolation method adopted (the Cresmann technique in this case) and the availability of a sufficient number of gauge stations uniformly distributed on the considered domain.

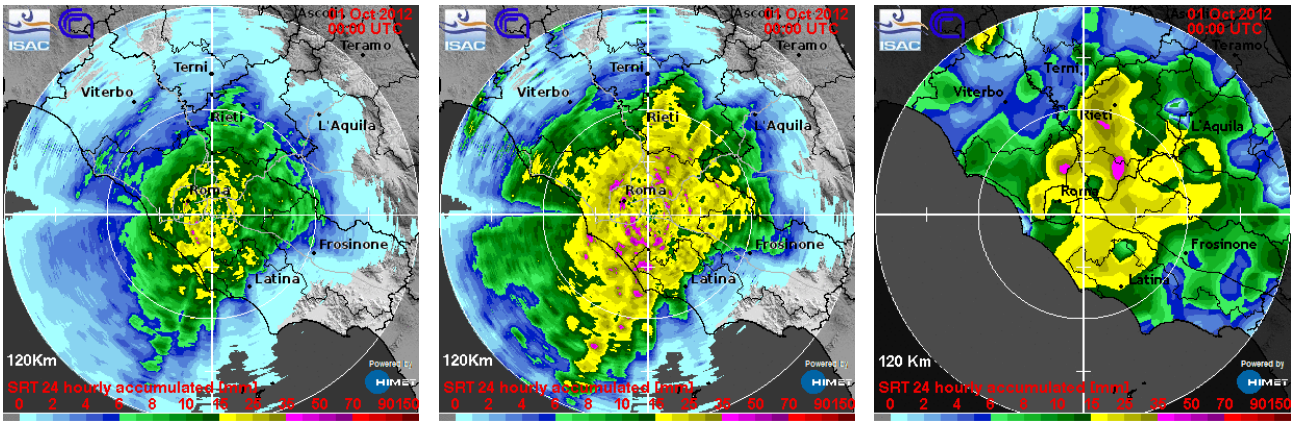

Figure 12: Impact of the correction chain on the 24h precipitation accumulation derived by MiniPolX data on 2012, Oct. 1 event. R_1 estimation (left panels), R_2 estimation (central panel) and daily interpolated accumulated rainfall derived from the available rain-gauge network (right panel) shown as qualitatively comparison.

6 Conclusions

A preliminary comparison of a new polarimetric mini-radar, named MiniPolX, against a benchmark polarimetric radar at X-band and C-band has shown promising results. MiniPolX can measure accurately the polarimetric observables, but it exhibits some problems related to the correlation coefficient at long ranges due to its wider beam with respect to other more performing systems such as the XPOL radar.

The chain of RAPP algorithms has been applied satisfactorily to MiniPolX, XPOL and Polar 55C observations and tested using a seven-month field campaign in the Roman area during HyMeX. Most of the error sources, affecting operational radar rainfall estimation, have been addressed. A combination of clutter-map polarimetric texture analysis is applied for the evaluation of data quality to suppress non meteorological echoes (i.e., ground clutter, clear-air echoes, and interferences caused by WLAN). Partial beam-blocking effects are accounted for by resorting to an electromagnetic propagation model based on a 240-m digital elevation model. A fairly efficient algorithm for differential phase measurement processing and

specific differential phase estimation is applied. Rain path attenuation effects are also handled through adaptive exploitation of differential phase measurements. A Bayesian hydrometeor classification, aimed at partitioning the radar volume in terms of microphysical hydrometeor categories, has been applied.
Rainfall estimation from MiniPolX, after RAPP proper processing, is generally in agreement with the rain gauge surface observations collected at ground during the campaign.
In conclusion, MiniPolX has shown to be a reliable low-cost solution for weather and flood monitoring at local scale. A network of X-band mini-radars might cover a broader area, particularly in complex terrain and urban scenario where operational systems exhibit observational gaps.

Acknowledgement

This paper has been produced with the financial assistance of the IPA Adriatic Cross-Border Cooperation Programme ADRIARadNet. The contents of this document are the sole responsibility of Cetemps and can under no circumstances be regarded as reflecting the position of the IPA Adriatic Cross-Border Cooperation Programme Authorities.

References

Bringi V.N. and Chandrasekar, V. Polarimetric Doppler Weather Radar: Principles and Applications, 2001, Cambridge, UK, Cambridge University Press

Ferretti R., Pichelli E., Gentile S., Maiello I., Cimini D., Davolio S., Miglietta M. M., Panegrossi G., Baldini L., Pasi F., Marzano F. S., Zinzi A., Mariani S., Casaioli M., Bartolini G., Loglisci N., Montani A., Marsigli C., Manzato A., Pucillo A., Ferrario M. E., Colaiuda V., and Rotunno R. Overview of the first HyMeX Special Observation Period over Italy: observations and model results, Hydrol. Earth Syst. Sci., 2014, Vol.18, pp.1953 - 1977,

Fulton R.A., Breidenbach, J.P., Seo, D., Miller, D. and O'Bannon, T. The WSR-88D rainfall algorithm, Wea. Forecasting, 1998, Vol. 13, pp. 377 - 395.

Gourley J.J. and Tabary P. and Parent du Chatelet J. Empirical estimation of attenuation from differential propagation phase measurements at C-band, J. Appl. Meteorol. Climatol., 2007, Vol. 46., pp. 306 - 317.

Kalogiros J., Anagnostou, M.N., Anagnostou, E.N., Montopoli, M., Picciotti, E. and Marzano, F.S. Optimum estimation of rain microphysical parameters from X-band dual polarization radar observables, IEEE Trans. Geosci. Remote Sensing, 2013, Vol. 51, n.5, pp. 3063 - 3076.

Kalogiros J., Anagnostou M.N., Anagnostou E.N., Montopoli M., Picciotti E. and Marzano F.S., Evaluation of a new polarimetric algorithm for rain-path attenuation correction of X-Band Radar observations against disdrometer data, IEEE Trans. Geosci. Remote Sens., 2014, Vol. 52, n.2, pp. 1369 - 1380.

Marzano F.S., G. Botta and M. Montopoli, Iterative Bayesian Retrieval of Hydrometeor Content from X-band Polarimetric Weather Radar, IEEE Trans. Geosci. Remote Sensing, 2010, ISSN: 0196-2892, Vol. 48, pp. 3059 - 3074.

McLaughlin D., Pepyne D., Chandrasekar V., Philips B., Kurose J., Zink M., Droegemeier K., Cruz-Pol S., Junyent F., Brotzge J., Westbrook D., Bharadwaj N., Wang Y., Lyons E., Hondl K., Liu Y., Knapp E., Xue M., Hopf A., Kloesel K., Defonzo A., Kollias P., Brewster K., Contreras R., Dolan B., Djaferis T., Insanic E., Frasier S. and Carr F., Short-Wavelength Technology and the Potential For Distributed Networks of Small Radar Systems. Bull. Amer. Meteor. Soc., 2009, Vol. 90, pp. 1797 - 1817

Mishchenko M.I. and Travis, L.D. Capabilities and limitations of a current Fortran implementation of the T-Matrix method for randomly oriented, rotationally symmetric scatterers., J. Quantitative Spectroscopy and Radiative Transfer., 1998, Vol. 60, n. 3, pp. 309 - 324.

Picciotti E., Gallese B., Cimoroni A., Montopoli M., Telleschi A., Volpi A., Consalvi F. and Marzano F.S. C-band radar precipitation measurements in mountainous region: comparison with raingauge fields and X-band radar data, Proceeding of the fifth European conference on radar in meteorology and hydrology ERAD 2008.

Straka, J.M., Zrnić, D.S. and Ryzhkov A.V. Bulk hydrometeor classification and quantification using polarimetric radar data: synthesis of relations., J. Appl. Met., 2000, Vol. 39, pp. 1341 - 1372.

Tabary P., Le Henaff, G., Dupuy P., Parent du Chatelet J. and Testud J. Can we use polarimetric X-band radars for operational quantitative precipitation estimation in heavy rain regions? In Proceedings of Weather Radar and Hydrology International Symposium. - Grenoble, 10-15 March 2008.

Vulpiani, G., Montopoli, M., Delli Passeri, L., Gioia, A., Giordano, P. and Marzano, F.S. On the Use of Dual-Polarized C-Band Radar for Operational Rainfall Retrieval in Mountainous Areas, J. Appl. Meteor. Climatol., 2012, Vol. 51, pp 405 - 425.